RSC Advances

PAPER

Cite this: *RSC Adv.*, 2024, **14**, 34985

AACVD synthesized tungsten oxide-NWs loaded with osmium oxide as a gas sensor array: enhancing detection with PCA and ANNs†

Alejandro Santos-Betancourt,[abc] Èric Navarrete,[a] Damien Cossement,[d] Carla Bittencourt[e] and Eduard Llobet*[abc]

Received 23rd July 2024
Accepted 25th October 2024

DOI: 10.1039/d4ra05346j

rsc.li/rsc-advances

This paper presents the fabrication of sensors based on tungsten trioxide nanowires decorated with osmium oxide nanoparticles using the aerosol-assisted chemical vapor deposition (AACVD) technique. This methodology allows the obtention of different osmium oxide decoration loadings on the tungsten oxide nanowires. The morphological and chemical characteristics; and the structural properties of the sensing layers of the sensors were studied using different techniques such as FESEM, HR-TEM, and ToF-SIMS. The gas sensing properties were analyzed for pure tungsten trioxide sensors and tungsten trioxide loaded with osmium exposed to nitrogen dioxide, hydrogen, and ethanol, thus assessing the impact of the loading on the sensor response. A sensor array comprising pure and osmium-loaded tungsten oxide devices coupled to multivariate pattern recognition techniques is shown to perform well in gas identification and quantification tasks, offering promising implications in the field of gas sensing technology.

1. Introduction

Global concern about air quality and the emission of toxic gases is increasing.[1] In that sense, significant progress has been made in developing sensors capable of detecting specific gases in different scenarios. Semiconductor metal oxides (MOXs) have emerged as a group of promising materials, favored for their small size, low manufacturing cost, and simple read-out-chain design.[2,3] Different material synthesis techniques can be envisaged for building a MOXs-based sensor, such as liquid-phase (LPS) and vapor-phase synthesis (VPS). One example of LPS is the sol–gel method, in which porous and thin sensing layers can be obtained.[4] Another example of this technique is hydrothermal growth.[5,6] This method enables obtaining different morphologies for the sensing layer, like nanoplates, nanowires, and nanorods.[7,8] On the other hand, VPS has approaches focused on chemical and physical methods. VPS is used to obtain nanomaterials (*e.g.*, nanoparticles, nanorods, *etc.*), and the thickness of the sensing layer can be controlled by optimizing the deposition temperature, the gas flow, the solvents, and the precursors.[9] One of the most used methods of VPS is aerosol-assisted chemical vapor deposition (AACVD).[10] This method combines the advantages of fine particle production in aerosol processes with the film-forming capabilities of CVD,[11] allowing the deposition of oxide structures like WO_3,[12] In_2O_3,[13] Co_3O_4,[14] Cr_2O_3,[15] CeO_2,[16] MgO,[17] MnO_2,[18] Al_2O_3,[19] CuO,[20] and Fe_2O_3.[21] When properly optimized, the AACVD enables also the loading of the aforementioned metal oxides with metal/metal oxide nanoparticles, thus showing good potential for the mass-production of functional nanomaterials. Since all these materials have specific characteristics and react to different chemical analytes, they are widely used as sensitive layers in sensors across numerous industries like automotive or petrochemical. Although MOXs are useful and effective for a long period, they have drawbacks such as lack of selectivity to specific gases, baseline drift, high sensitivity to humidity, and high operating temperatures.[22,23] In that sense, many metal oxides have been modified by doping or loading with other materials to address issues associated with their disadvantages.[24–28]

Doping metal oxides with metal ions (*e.g.*, Ti^{3+}, Sm^{3+}, La^{3+}, Ce^{3+}, Pr^{3+}, Cr^{3+}) has been exploited as a way to tune band-gap, charge carrier concentration, carrier mobility and defects, resulting in increased responsiveness to gases.[29–32] Metal oxides loaded with metal catalyst nanoparticles have been widely used to increase the sensitivity and adjust the selectivity of gas

---

[a] *Universitat Rovira i Virgili, Microsystems Nanotechnologies for Chemical Analysis (MINOS), Departament d'Enginyeria Electronica, Països Catalans, 26, 43007 Tarragona, Catalunya, Spain*

[b] *IU-RESCAT, Research Institute in Sustainability, Climatic Change and Energy Transition, Universitat Rovira i Virgili, Joanot Martorell 15, 43480 Vilaseca, Spain. E-mail: eduard.llobet@urv.cat*

[c] *TecnATox - Centre for Environmental, Food and Toxicological Technology, Universitat Rovira i Virgili, Avda. Països Catalans 26, 43007 Tarragona, Spain*

[d] *Materia Nova Research Center, Parc Initialis, Avenue Copernic 3, 7000 Mons, Belgium*

[e] *Chimie des Interactions Plasma – Surface (ChIPS), Research Institute for Materials Science and Engineering, Université de Mons, Parc Initialis, Avenue Copernic 3, 7000 Mons, Belgium*

† Electronic supplementary information (ESI) available. See DOI: **https://doi.org/10.1039/d4ra05346j**

sensors. These nanoparticles contribute to chemical sensitization by enhancing the amount of reactive oxygen species adsorbed[33–35] on the semiconductor metal oxide surface and/or by helping break down target molecules by catalytic effects, thereby enhancing their reaction with oxygen through spillover effects.[36] Additionally, recent advancements have led to the creation of single-crystalline, nanostructured metal oxides, such as nanorods and nanowires.[11,26,27,37] Metal nanoparticles (NPs) may also have an electronic sensitization effect *via* developing heterojunctions at the metal oxide/NP interface.[38–40] In particular, combining n-type metal oxide nanowires decorated with p-type metal oxide NPs results in multiple n-p heterojunctions, causing significant electronic sensitization effects.[41] As n–p heterojunctions form, electrons move from the n-type metal oxide to the p-type nanoparticles, creating depletion zones. The adsorption of gases onto these nanoparticles triggers further electronic charge transfers to the n-type metal oxide base, altering the depletion zone width and significantly changing the film's overall electrical conductance, thus giving readable data linked to the target gas. In the literature, the most used p-type nanoparticles are the ones based on noble metals due to their excellent chemical properties, stability, and performance. While the most employed metal NPs are Pt, Pd, and Au, in the last few years we have studied the use of other transition metal NPs such as Ir,[26] Co,[27] or Ni.[28] Supported on tungsten oxide nanowires. In addition, the literature shows only few papers in which MOXs have been loaded with osmium. Capone *et al.*[42] developed a sensor consisting of SnO_2 decorated with osmium using the sol–gel technique to detect methane at a low working temperature. Quaranta *et al.*[43] used an array of sensors including a pristine SnO_2 sensor and decorated ones with palladium, platinum, and osmium. They analyzed the data using a multivariate approach and used principal component analysis (PCA) to discriminate gaseous species such as carbon monoxide, methane, ethanol, methanol, and nitrogen dioxide. Considering the scarce number of results available on osmium loaded MOX gas sensors, the study of osmium supported on WO_3 seems novel and worthwhile.

It is known from the literature that using gas sensor arrays and chemometrics is a way to enhance the discrimination and quantification ability of individual MOX sensors.[44,45] In this approach, sensors with overlapping selectivity are coupled to multivariate data analysis techniques that process sensor response vectors.[46–48] In particular, the principal component analysis (PCA), a technique that enables building models that maximize the data variance explained (*i.e.*, sensor response variance), has been widely employed as an unsupervised dimensionality reduction and classification technique in gas sensor arrays. Besides enabling data separation and classification, PCA allows for studying how individual sensors contribute to gas discrimination and helps identifying redundant or irrelevant sensors.[47,49] Additionally, artificial neural networks (ANNs) such as the feed-forward multi-layer perceptron (FF-MLP) have been widely employed in quantitative analysis (*e.g.*, to predict gas concentrations). The MLP is a supervised method that learns the intricate patterns and relationships existing between the sensor array responses.[50,51] In this paper, pristine tungsten trioxide (WO_3) and WO_3-based sensors loaded with two levels of osmium oxide concentrations are synthesized for the first time using the AACVD technique. The synthesized sensors were employed in a sensor array to discriminate and quantify chemical species such nitrogen dioxide, ethanol, and hydrogen. The output data from the sensor array was processed through PCA and the multilayer perceptron (MLP) ANNs of studying the discrimination and quantification ability of the sensor system.

2. Experimental

2.1 Description of the fabrication process

Tungsten trioxide (WO_3) nanowires (NWs) and tungsten trioxide loaded with osmium oxide (WO_3/OsO_4) were synthesized through the AACVD at 375 °C. The nanomaterials were grown on top of commercially available alumina substrates, from CeramTech GmbH, that present screen-printed 300 μm gap interdigitated platinum electrodes on the top side and an 8 Ω heating platinum resistor on the bottom side. The AACVD process was performed in two steps. First, the synthesis of pristine WO_3 NWs and then, the loading of the WO_3 NWs with osmium at different concentration levels. To grow the pure WO_3 NWs, as indicated in Fig. 1, 40 mg of tungsten hexacarbonyl $W(CO)_6$, (Sigma Aldrich, St. Louis, MO, USA, CAS: 14040-11-0) as an organometallic precursor was weighted. Subsequently, the precursor was solubilized in a mixture of methanol (Scharlab, Sentmenat, Spain, CAS: 67-56-1) and acetone (Sigma Aldrich, St. Louis, MO, USA, CAS: 67-64-1) with a 1 : 3 volume ratio (5 mL and 15 mL, respectively). The solution was sonicated using an ultrasonic cleaning machine, SKE-3S (Tangshan UMG Medical Instrument Co., Ltd, Tangshan, Hebei, China) until all the precursor material was fully dissolved (around 15 minutes) and then, placed in an aerosol generator bath (Miniland Humiplus Advanced, Ultrasonic, PO: POD-MNL 15-02435), which generates 1 MHz ultrasonic waves to convert the solution into a micro-droplet aerosol. This aerosol is carried *via* a pipe system using nitrogen as an inert carrier gas at a constant flow of 1 L min^{-1} towards a preheated CVD hot-wall reactor at 375 °C where the alumina substrates were previously introduced. The resulting WO_3 NWs layer fully coats the electrodes and, as typically, some amorphous carbon remnants are left by the organic precursor and solvents. To remove such impurities and enhance the oxidation stoichiometry, an annealing process is performed right after the deposition, which is conducted in a Carbolite CWF 1200 muffle (Carbolite Gero Ltd, Neuhausen, Germany) at 500 °C for 2 h, with a temperature ramp of 5 °C min^{-1}, under pure dry air. Fig. 1 describes a schematic of the process.

Afterward, a second AACVD process was conducted to achieve two different levels of osmium loading (low and high concentrations). In this second step, two amounts of osmium were weighted using a KERN (KERN & SOHN GmbH, Germany) 0.0001 g precision balance: 2.5 and 10 mg of osmium(III) chloride hydrate ($OsCl_3 \times H_2O$) (Sigma Aldrich, St. Louis, MO, USA, CAS: 13444-93-4), subsequently, two methanol 10 mL solutions were prepared. The AACVD process was repeated, as described before, in this case, the previously annealed substrates were placed again inside the CVD reactor and preheated at 350 °C respectively in

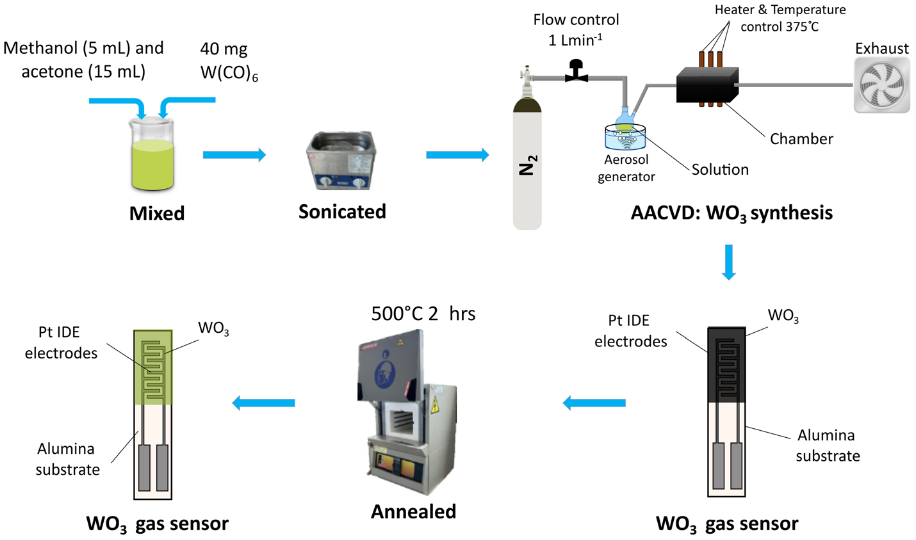

Fig. 1 Block diagram AACVD synthesis of WO_3 sensors.

two separate runs. The processes result in two WO_3/OsO_4 samples at different loading levels: WO_3/OsO_4/2.5 mg and WO_3/OsO_4/10 mg. Finally, an annealing process was performed to clean the remnants of carbon from the surface of the films.

2.2 Material characterization

Field Emission Scanning Electron Microscope (FESEM) Scios 2 DualBeam was used to study the surface morphology of the sensitive layers. Sample characterization was performed at a high vacuum, and the electron acceleration voltage was established between 2 and 5 kV. Also, the energy-dispersive X-ray (EDX) incorporated in the FESEM Scios was used to check the chemical composition of the active layers. HR-TEM characterization of the samples was performed on a Jeol 2100 microscope, working at 200 kV. The material was scratched from the alumina substrate and dispersed in methanol. The

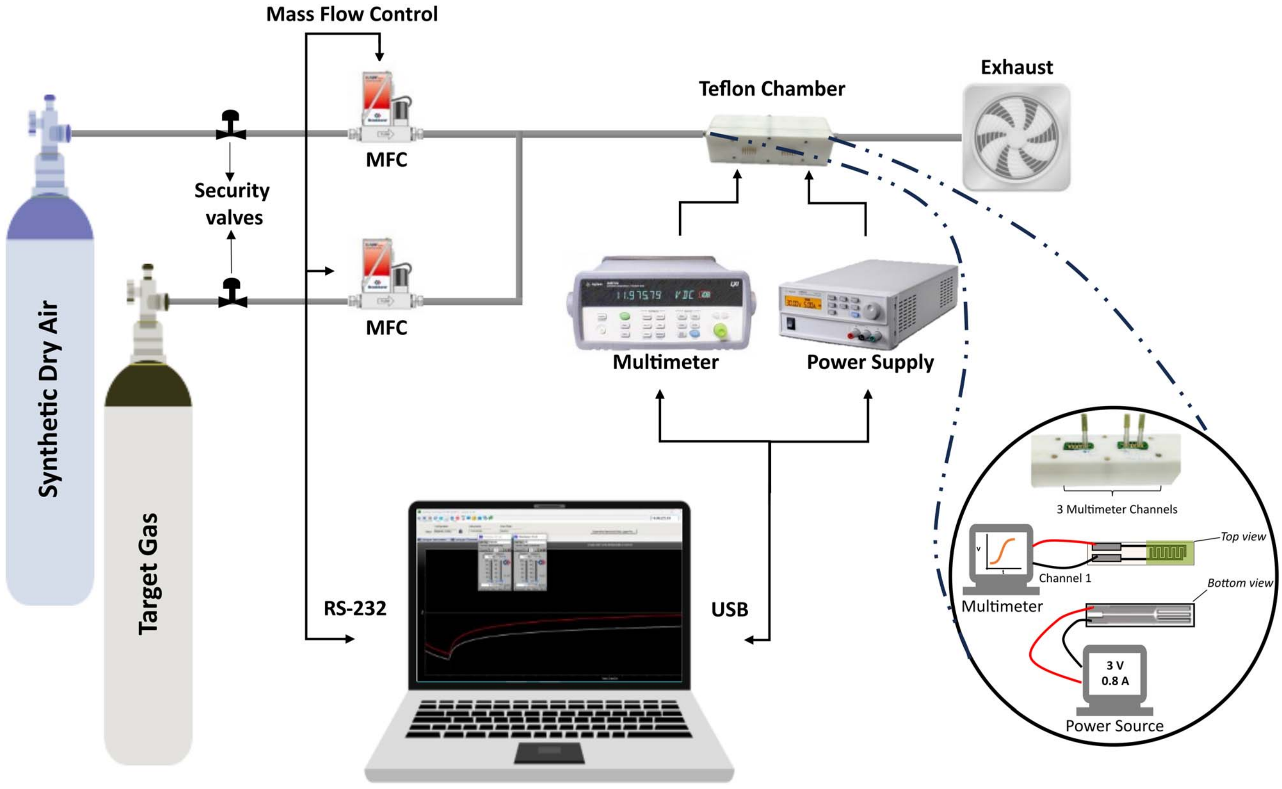

Fig. 2 Schematic representation of the gas measurement system.

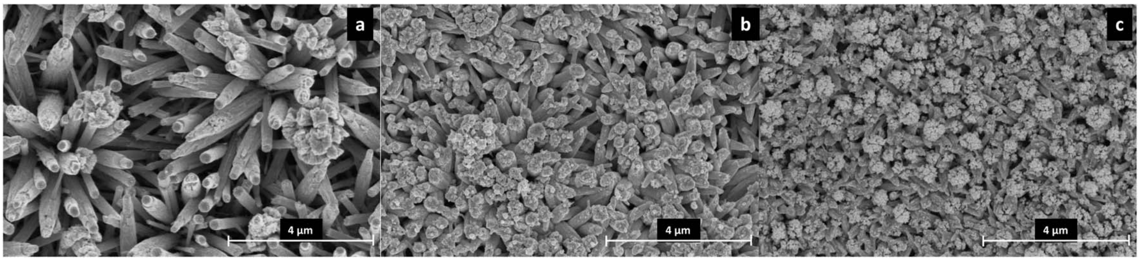

Fig. 3 FESEM at 4 µm of sensors. (a) Pure WO_3 (b) WO_3/OsO_4 (2.5 mg) (c) WO_3/OsO_4 (10 mg).

dispersion was ultrasonicated for 20 minutes and a drop was deposited on a lacy carbon film supported by a nickel grid. Also, using the same equipment, EDX analysis was performed. Likewise, before ToF-SIMS data acquisition, samples were pre-cleaned with a giant argon cluster beam ($Ar_{3000}{}^{+}$) operated at 10 keV over an area of 500 × 500 µm^2, gently removing surface hydrocarbon contamination while keeping the underlying sensor material intact. At the center of the freshly prepared sputter crater, surface ToF-SIMS spectra were acquired in positive mode using a ToF-SIMS M6 instrument from ION-TOF GmbH, Münster, Germany. A Bi^+30 keV primary ion beam was used at a current of ∼0.76 pA and was rastered over a scan area of 200 × 200 µm^2, for 1000 seconds, allowing the sensitivity in the detection of Os^+ to be enhanced.

2.3 Description of the measurement system

The gas-sensing properties of the different sensors were studied. The sensors were exposed to different gases both reducing; ethanol vapors (EtOH) and hydrogen (H_2), and an oxidizing gas as nitrogen dioxide (NO_2). The concentrations analyzed for ethanol vapors were 5, 10, 15, and 20 ppm; for hydrogen 250, 500, 750, and 1000 ppm; and the concentrations were set for nitrogen dioxide in 250, 500, 750, and 1000 ppb. To do so, the sensors were placed inside an airtight Teflon® chamber with an inner volume of 21.18 cm^3. The chamber has a connector-type edge dual female 12POS 0.100 FMC06DRYH (©2024 Sullins Connector Solutions, San Marcos, CA 92069, USA) which interfaces the sensors with the measurement instrumentation. Different gases were

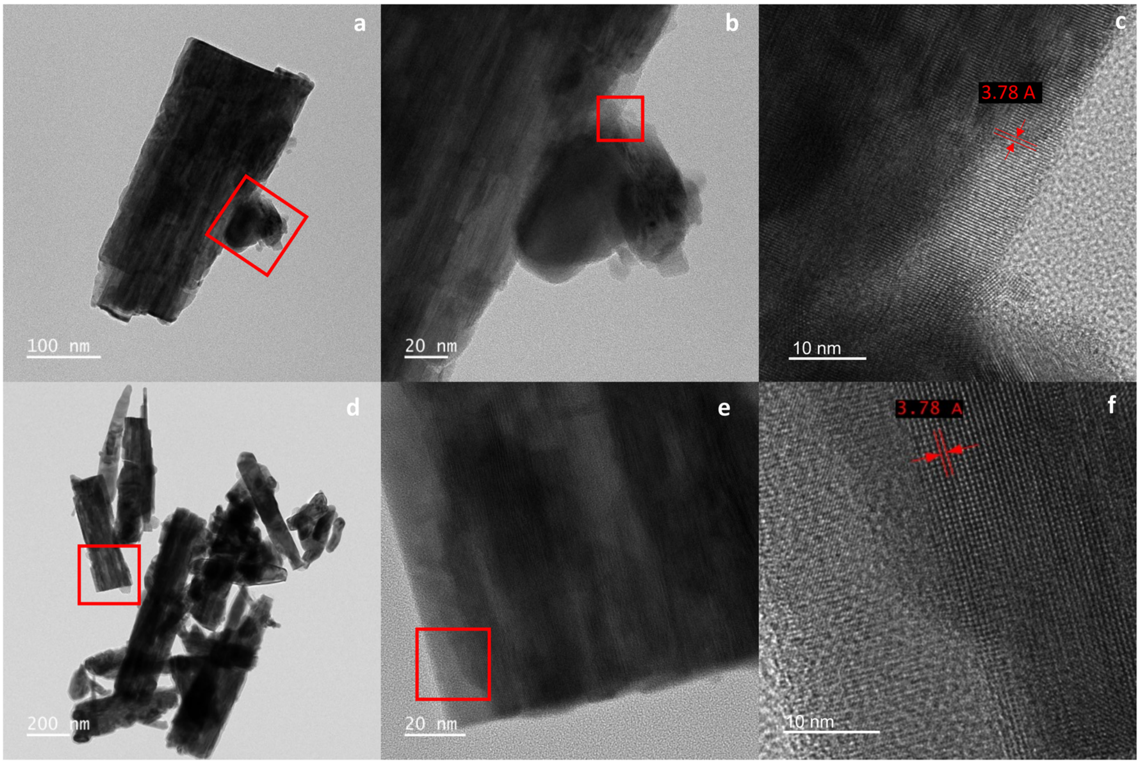

Fig. 4 (a) Broken nanowires, WO_3/OsO_4/2.5 mg, from the sonication process during sample preparation. (b) HR-TEM inset from a nanowire body image, WO_3/OsO_4/2.5 mg, the caption shows the interplanar structure, probing a high crystallinity. (c) Close up, WO_3/OsO_4/2.5 mg, showing the (002) interplanar distance of WO_3 (d) broken nanowires, WO_3/OsO_4/10 mg, from the sonication process during sample preparation. (e) HR-TEM inset from a nanowire body image, WO_3/OsO_4/10 mg, the caption shows the interplanar structure, probing a high crystallinity. (f) Close up, WO_3/OsO_4/10 mg, showing the (002) interplanar distance of WO_3.

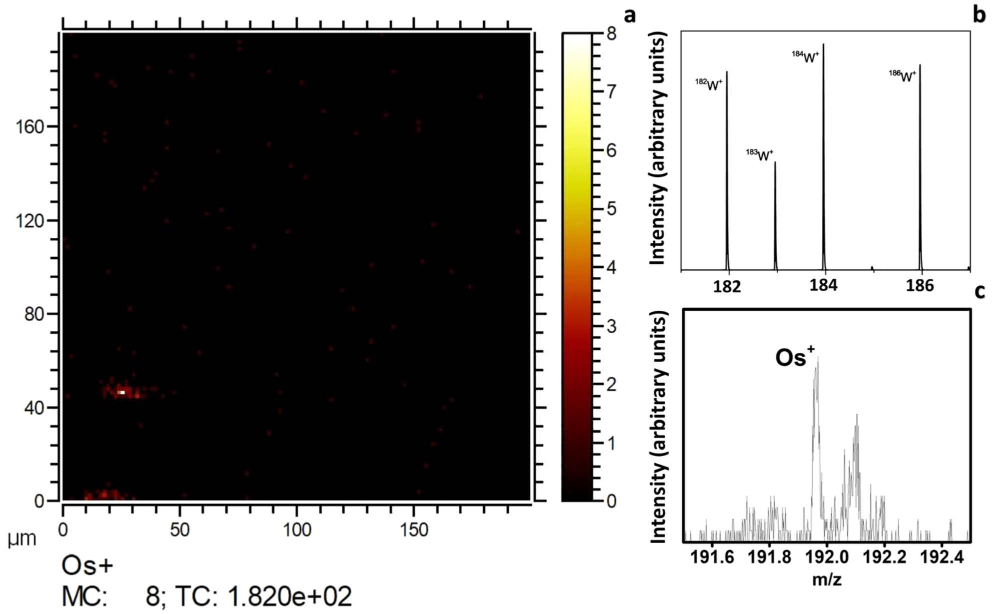

Fig. 5 ToF-SIMS analysis results for a WO_3/OsO_4/10 mg sample. (a) Chemical mapping image of the surface with osmium clusters appearing as red dots/areas, (b) spectrum associated to tungsten detection, and (c) spectrum associated to osmium detection.

delivered to the chamber through a computer-controlled mass-flow system to ensure the reproducibility of the concentrations and constant flow. The gases were purchased from Linde® as calibrated gas bottles balanced in dry air and the carrier gas was zero-grade dry synthetic air. The analysis of the gases was programmed as pulses: consisting of increasing target gas concentrations in between of dry air supplying to recover the baseline at a constant flow of 100 mL min^{-1}. The sensor resistance was measured and stored employing a Keysight 3972A data acquisition system. An Agilent U8001A Single Output DC Power

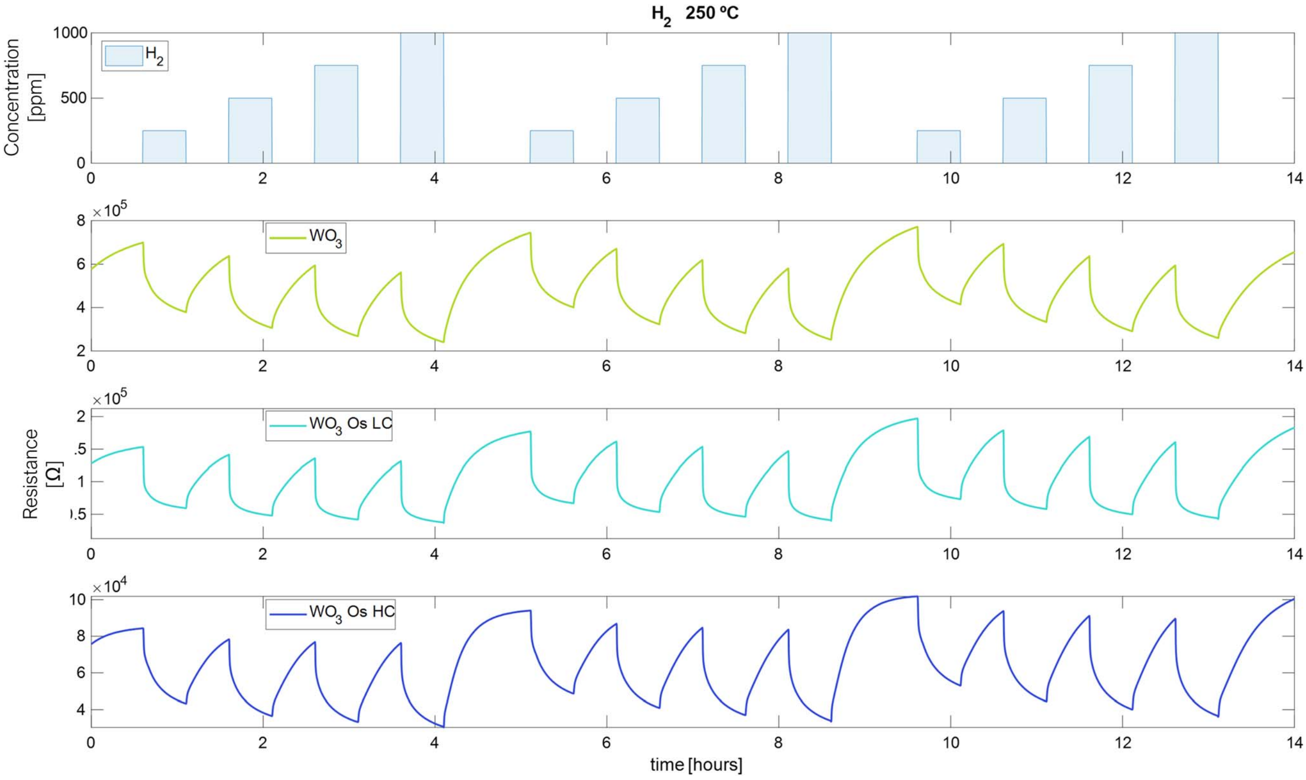

Fig. 6 Measurement of the sensor at an operating temperature of 250 °C throughout H_2 exposures.

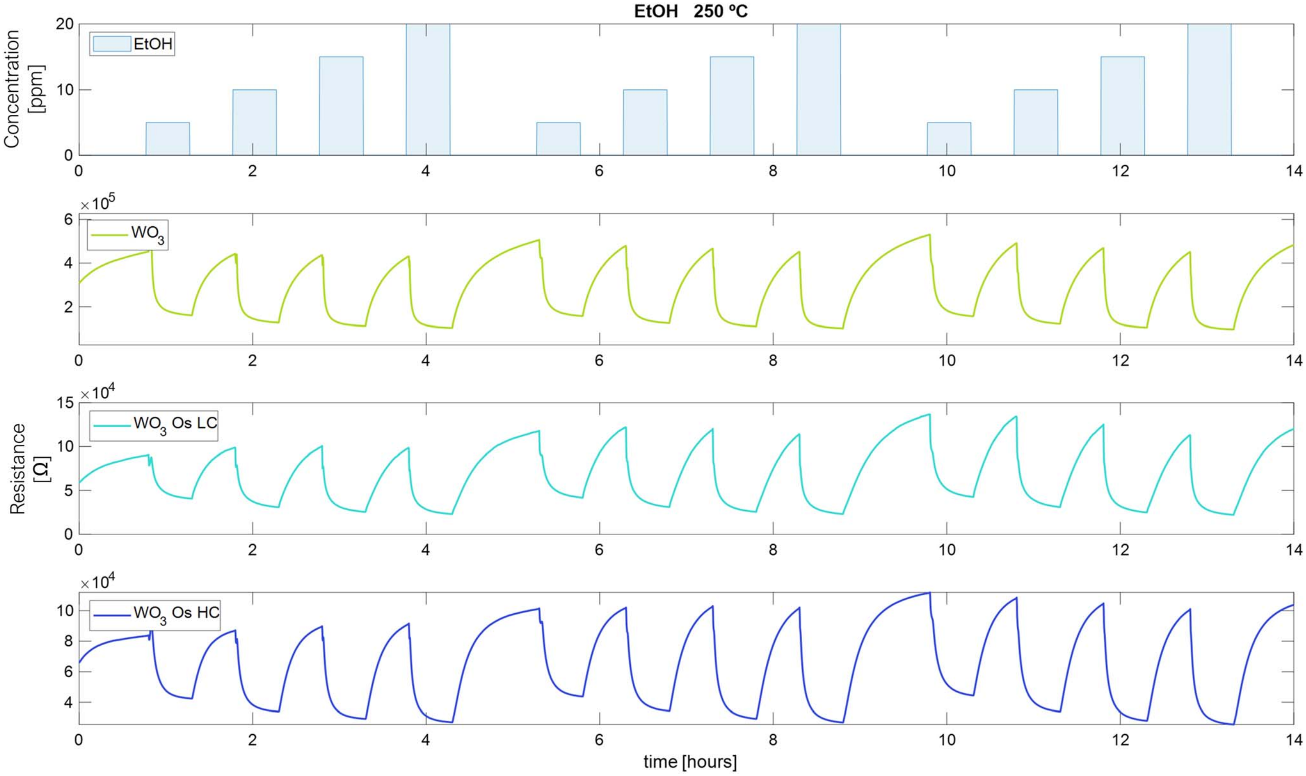

Fig. 7 Measurement of the sensor at an operating temperature of 250 °C throughout EtOH exposures.

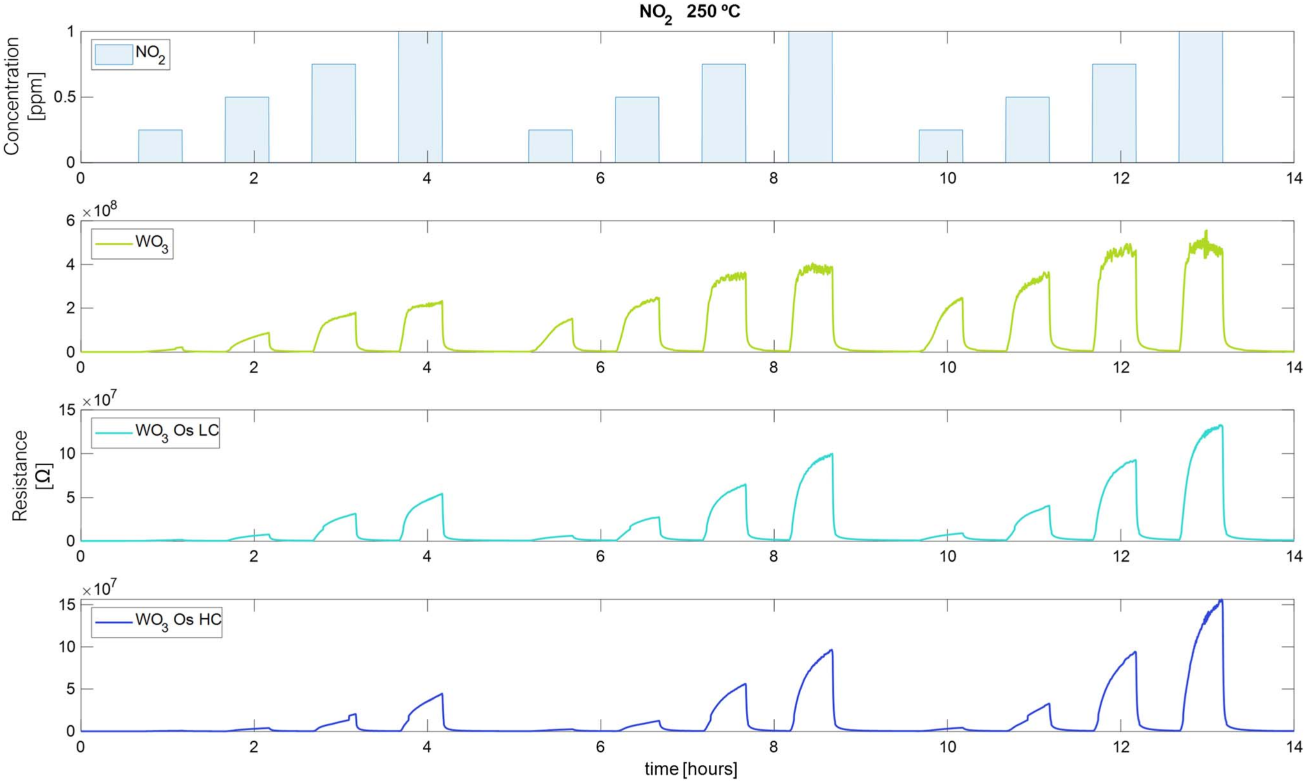

Fig. 8 Measurement of the sensor at an operating temperature of 250 °C throughout NO$_2$ exposures.

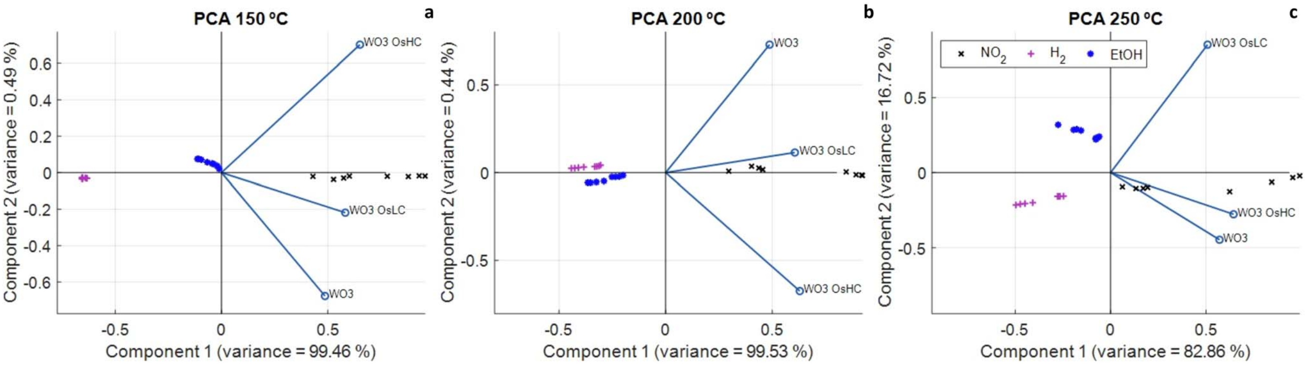

Fig. 9 PCA at (a) 150 °C, (b) 200 °C, and (c) 250 °C.

Supply was used to power the heating element of the substrates to achieve the operating temperatures of 150 °C, 200 °C, and 250 °C. This system is depicted in Fig. 2.

2.4 Methodology for data analysis

After measuring the resistance variation of each sensor while reacting with the target gas, specific values were selected from the measurement dataset. The electrical resistance values were taken before and after each pulse of the target gas. Then, the electrical resistance values related to pulses of the same concentration were averaged and PCA was conducted to classify the gases. On the other hand, using the whole dataset of measurements, MLPs were trained, using MATLAB Statistics and Machine Learning Toolbox (academic-available license). Before that, the sensor array raw data was filtered using an asymmetric windowed filter with a left-right length of 12 and 0 samples. Then, the resulting data served as features (input layers) to develop the MLP models. For training the MLPs, 80% of the observations were used, and the remaining 20% were reserved for testing. Training and validation vectors were selected randomly for these purposes. A 5-fold cross-validation scheme was used to avoid overfitting during the training process. The tuning process compared different types of architecture (hidden layers), varying the number of layers (1, 2, 3) and neurons per layer (10, 25, 100). The quantification MLP with best performance was selected based on root mean squared error (RMSE) and coefficient of determination (R^2). Prediction accuracy was the criterion employed for evaluating the performance of MLP classification models. Once the architecture of the MLP was set, the activation function was varied (including none: $f(x) = x$, ReLU: $f(x) = \max(0, x)$, sigmoid: $f(x) = \frac{1}{1+e^{-x}}$, and Tanh: $f(x) = \frac{2}{1+e^{-2x}} - 1$) to determine the best option.

3. Results & discussion

3.1 Sensing layer characterization

Fig. 3 shows FESEM images for the different sensors fabricated, pure WO_3 NWs and WO_3/OsO_4.

There is a clear change in the surface morphology as the concentration of osmium increases (see Fig. 3a–c). The pure WO_3 NWs surface shows a smooth surface with well-defined nanowire tips and bodies. As the concentration of osmium increases, the formation of material clusters also increases. The presence of osmium particles could lead to a displacement of material from the already formed layers acting as a seed thus enhancing the nucleation of material around the tips of the nanowires. One major effect of such change in the layer is the increase in the total surface area available for the oxygen species to adsorb and react. Similarly, a sample of the synthesized layer was brought to the HR-TEM to study and determine the crystallinity and composition. Fig. 4 shows a cluster of WO_3/OsO_4/2.5 mg and WO_3/OsO_4/10 mg NWs with an inset depicting that the *d*-spacing between lattice fringes in the inset is 3.78 Å corresponding to (002) planes in WO_3 with monoclinic $P\bar{1}$ structure (ICDD 43e1035), confirming the composition of the tungsten trioxide nanowires. EDX studies were carried out on the sensor samples (*i.e.*, on alumina substrates) and on the samples prepared for TEM analysis (*i.e.*, on TEM grids). These studies (see Fig. S1 and S2 in the ESI†) could not confirm the presence of osmium in loaded samples. The amount of osmium loading achieved remains under the detection limit of the technique.

On the other hand, Fig. 5 shows the ToF-SIMS analysis on a WO_3/OsO_4/10 mg sample. The presence of the Os^+ peak was observed at *m*/*z* 191.96. It is noteworthy to point out that the Os^+ peak region, features a higher background compared to the W^+ peaks, which suggests that osmium occurs with very low abundance. In conclusion, ToF-SIMS has confirmed that osmium is present in loaded samples. Beyond the detection of Os^+ in the ToF-SIMS spectra, simultaneously with the spectra acquisition chemical images were recorded of the surface sample, enabling the location of osmium. ToF-SIMS was used instead of XPS because the former technique is more sensitive than the latter. This aspect is discussed further in the ESI.†

3.2 Gas measurement results

The measurements of the electrical resistance of each sensor are shown in Fig. 6–8. Sensors were operated at 250 °C, in which the sensors showed the best response intensity and response dynamics to the target gases. Long-term measurements for the operating temperatures of 150 °C and 200 °C can be found in Fig. S3 and S4 in the ESI.† Fig. 6 to 8, report the responses to

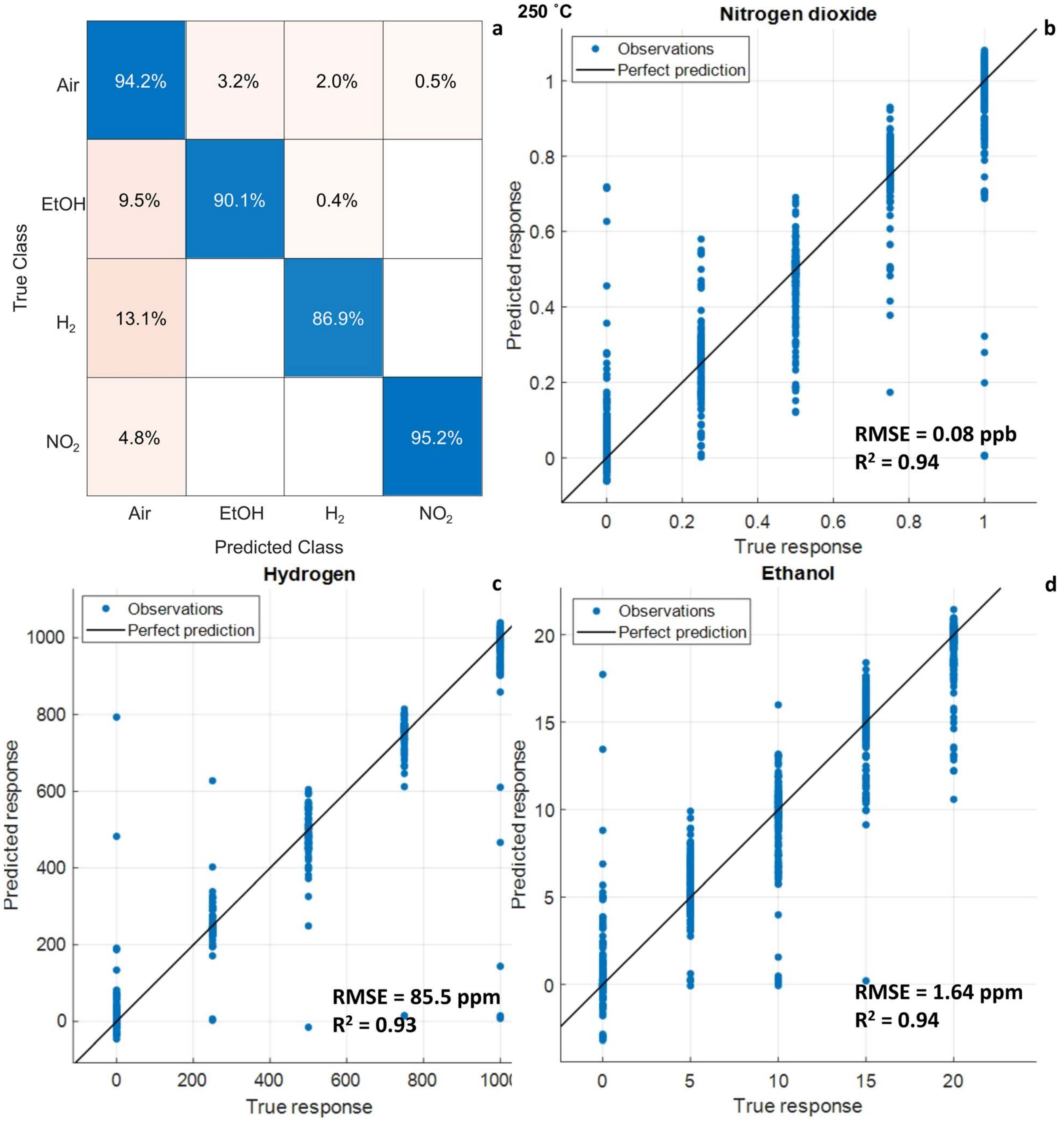

Fig. 10 Results of the classification (a) and quantification models NO_2 (b), H_2 (c) and EtOH (d). Input data is from the three-sensor array. Sensors were operated at 250 °C.

three repeated cycles of four increasing pulsed concentrations of the target gases. Each pulse of gas lasted 30 minutes and was followed by 30 minutes of dry air to recover the baseline. For H_2 and EtOH, the resistance of the sensors decreases but in the case of NO_2, the resistance value increases, as expected for an n-type semiconducting nanomaterial.

This measurement protocol enabled testing the repeatability of measurements. Fig. S5a–c in the ESI† show the calibration curves for H_2, EtOH, and NO_2 at 250 °C, respectively. Also, they show the mean of the responses of the three repeated cycles in each concentration of the target gases and the error bars corresponding to their variability (or measurement uncertainty). It is noticed that the response increases while the concentration of gases increases. For H_2, Fig. S5a,† the pristine WO_3 sensor increases its measurement uncertainty when increasing the gas concentration from 0.18% to 0.4% (Table S1 in the ESI† shows numerical details). While the sensors loaded with osmium keep this uncertainty almost constant throughout the concentration range studied (WO_3/OsO_4/2.5 mg: from 0.76% to 0.66%, WO_3/OsO_4/10 mg: from 0.4% to 0.37%). It can also be noticed that, for H_2 detection, the two doped sensors show a higher response than the pristine sensor (Fig. S5a†). The response of the sensors towards EtOH is shown in Fig. S5b.† The sensor with the lowest load of osmium behaves similarly to the pristine sensor. The sensor with higher loadings of osmium shows the lowest response. For the three sensors, the measurement uncertainty decreases as the gas concentration increases (WO_3: from 3.1% to 1.2%, WO_3/OsO_4/2.5 mg: from 7.2% to 2.1%, WO_3/OsO_4/10 mg: from 5.6% to 2.1%). When analyzing the response of the sensors towards NO_2, it is worth noticing that the sensor with the higher loading level of osmium shows the highest sensitivity (*i.e.*, slope of the calibration curve). The measurement uncertainty associated to the detection of NO_2 is also higher (Fig. S5c and Table S1 in the ESI†). Considering these results, the tungsten oxide sensors loaded with osmium hold promise for the detection of hydrogen and nitrogen dioxide.

The effect of loading tungsten oxide on the detection mechanism is as follows. As the amount of osmium loading is increased, the nanowires show an increased number of clusters of tungsten oxide along their body, thus becoming more defective. As a result, the number of available sites where oxygen can be adsorbed is enhanced with osmium oxide loading. The defects present on the material surface act as highly active sites compared to the pristine regions of tungsten oxide. These active sites break the uniform atomic lattice of the nanowire smooth body (see Fig. 3), creating areas with unsaturated bonds, unpaired electrons, or localized charge variations. We postulate that the number of such defects increase with the amount of osmium loaded, acting as adsorption sites for oxygen molecules, which subsequently react with the target gas. The defects act as electron donors or acceptors, depending on their, nature helping to reduce the activation energy required for adsorption and subsequent reaction steps. When oxygen adsorbs at these defect sites, it captures electrons. These reactive oxygen species are chemically active and are ready to interact with the target gas molecules, facilitating the chemical reactions that are responsible for the sensing response.

3.3 Data analysis

Given the fact that the different sensors studied show overlapping selectivity, a multivariate analysis was performed in the next sections to assess whether or not the discrimination of the chemical species considered and their quantification could be achieved. A 3-element sensor array, which comprised pristine, low osmium loaded and high osmium loaded tungsten oxide sensors was considered for this analysis.

Fig. 9a–c show the Biplot of a principal component analysis performed using the electrical resistance values of the three sensors. A PCA analysis was performed for every operating temperature tested. Results denote that the different gases can be discriminated, no matter the operating temperature, through a simple visual inspection. This indicates that, even though individual sensors show cross-responsiveness to the different chemical species considered, a simple, linear pattern recognition algorithm such as PCA that processes the responses of the three sensors together, achieves good discrimination performance.

Likewise, MLPs were trained using the whole dataset of measurements divided into the three temperatures. To discriminate the gases, the output labels of the models were separated into air, ethanol, hydrogen, and nitrogen dioxide. Table S2 in the ESI† shows the performance of the trained classification algorithms. At 250 °C, the classification model with the highest accuracy consists of one hidden layer with 10 neurons and utilizes Tanh as the activation function. The total accuracy obtained during training was approximately 91.6%, while during the test with the observations left out for this purpose, the total accuracy was 93.18%. The confusion matrix for the test data is shown in Fig. 10a. The classification accuracy was greater than 94% when supplying dry air to the sensors, 90.1% for ethanol, 86.9% for hydrogen, and 95.2% for nitrogen dioxide. It is worth mentioning that classification errors occur mostly between target gases and air (ex: when supplying ethanol, the algorithm misclassifies 9.5% of ethanol samples as air and only 0.4% as hydrogen). There is almost no confusion among the target gases. Similarly, models were trained to quantify the gases. Tables S3–S5 in the ESI† compare the results according to RMSE and R^2 for NO_2, EtOH, and H_2, respectively. For NO_2 at 250 °C, the best model comprised three hidden layers, 10 neurons per layer, and ReLU as the activation function. This model results in an RMSE of 0.08 ppb and R^2 of 0.94 for the samples left out for testing. Fig. 10b shows the predicted *vs.* true values at 250 °C for the test data. For the quantification of hydrogen at 250 °C, the best model used one hidden layer, 100 neurons per layer, and ReLU as the activation function. The RMSE increases to 85.57 ppm but is still a good result, since the measured concentration range for H_2 is up to 1000 ppm. The R^2 value is 0.94, see Fig. 10c. In the case of ethanol, the best model had three hidden layers, 10 neurons per layer, and Tanh as the activation function. For test data, RMSE was 1.64 ppm and R^2 was 0.94, see Fig. 10d.

At 200 °C, the classification accuracy was greater than 92% when classifying air, 89.4% for ethanol, 82.2% for hydrogen, and 96.1% for nitrogen dioxide, see Fig. S6a.† The best quantification model for NO_2 had one hidden layer, 100 neurons per layer, and ReLU as the activation function. It gave as a result an RMSE of 0.11 ppb and R^2 of 0.89 for test data. Fig. S6b† shows the predicted *vs.* true values at 200 °C for the test data. For the quantification of hydrogen at 200 °C, the best model also had one hidden layer, 100 neurons per layer, and ReLU as the activation function. Fig. S6c† shows the result for test data, RMSE of 107.92 ppm and the R^2 0.90. Fig. S6d† shows the test results of the best model for ethanol quantification. The model comprised three hidden layers, 10 neurons per layer, and Sigmoid as the activation function. RMSE was 1.27 ppm and R^2 was 0.96 for test data. Results at 150 °C are displayed in Fig. S7.† Classification accuracy of 97.4% for air, 81.4% for ethanol, hydrogen 73.5%, and 96% for NO_2 was achieved, see Fig. S7a.† The best prediction model for ethanol comprised one hidden layer, 100 neurons per layer, and Tanh as the activation function. For predicting nitrogen dioxide, the best model comprised three hidden layers, 10 neurons per layer, and Tanh as the activation function. For hydrogen, the quantification model comprised one hidden layer, 100 neurons per layer, and ReLU as the activation function. The results of test data are presented in Fig. S7 in the ESI.†

The operating temperature of the sensors impacts the performance achieved by the discrimination and the quantification models. If the sensor operating temperature decreases, accuracy decreases when classifying reducing gases. On the other hand, when classifying an oxidizing gas like NO_2, the classification accuracy barely changes when the working temperature of the sensors is decreased within the temperature range studied. This is summarized in Table S6 in the ESI.† This behavior could be used to reduce power consumption when classifying NO_2. Moreover, quantification results show that the best performance is reached at higher operating temperatures. Table S7† summarizes the best model for quantifying each target gas at different working temperatures.

The metrics (accuracy, R-squared, and RMSE) of the models built to discriminate and quantify the target gases are comparable or even better than those of the state of the art.[52] Additionally, Table S8† enables the comparison of the results achieved with some recent results from the literature.

4. Conclusions

The AACVD technique has been employed in a two-step process to successfully grow tungsten oxide nanowires pure and loaded with two amounts of osmium oxide nanoparticles. FESEM and HR-TEM analysis has verified that the synthesized materials were crystalline, and the loading of osmium impacted the layer morphology. Despite being unable to determine the presence of osmium nanoparticles through microanalysis (EDX), the ToF-SIMS analysis confirms the presence of osmium on loaded samples, yet at trace levels. The gas-sensing properties of the obtained nanomaterials have been successfully studied under the presence of nitrogen dioxide, hydrogen, and ethanol at ppb and ppm levels. It was found that osmium loaded sensors hold promise for the detection of H_2 and NO_2.

Additionally, the response data from the three sensors was processed using two different multivariate techniques such as PCA and MLP. These results show that a 3-element sensor array, made of cross-responsive sensors, is able to discriminate and quantify the target gases with good accuracy. Particularly, the processing of the sensor array data using artificial neural network models allowed for reaching a high discrimination ability (H_2: > 86%, EtOH > 90%, and NO_2: > 96%) and a good quantification ability ($R^2 \sim 0.94$) on validation data that had not been used for training.

Despite our results show that the multivariate data analysis approach enhances the selectivity and quantification ability of the cross-responsive, pure and osmium loaded tungsten oxide sensors, further research is needed. For instance, the optimization of the amount of osmium in the loading process of each sensor should help enhancing sensor performance. This will require a careful optimization of the AACVD process, which has resulted in low loading levels. Also, performing new measurements for a longer period than the 2 months measurement period reported here would help understanding how the sensors age, and evaluating their long-term stability.

Data availability

The data related to this manuscript is publicly available from the Zenodo repository (**https://zenodo.org/**) under the DOI: **10.5281/zenodo.12800041**.

Author contributions

A. S.-B.: investigation, formal analysis, data curation, visualization, writing—original draft; E. N.: conceptualization, methodology, validation, writing—review & editing; D. C.: resources, data curation; C. B.: writing—review & editing, resources, validation; E. L.: writing—review & editing, supervision, funding acquisition.

Conflicts of interest

The authors declare no conflicts of interest.

Acknowledgements

The authors want to acknowledge Sergi Plana Ruiz for his help in performing the HR-TEM analysis. This work was supported in part by EU in the framework of H2020-MSCA-RISE-2018: Marie Sklodowska-Curie Actions, grant 823895-PE; MICINN, grants PDC2022-133967-I00 and TED2021-131442B-C31, as well as AGAUR grant 2021 SGR 00147. A. S.-B. is funded by the E. U. Horizon 2020 research and innovation programme under the Marie Skłodowska-Curie grant agreement no. 945413 and from the Universitat Rovira i Virgili (URV). C. B. is a research associate of FNRS-Belgium. E. L. is supported by the Catalan Institution for Advanced Studies *via* the 2023 Edition of the ICREA Academia Award.

References

1 Monitoring air pollution levels is key to adopting and implementing WHO's Global Air Quality Guidelines, **https://www.who.int/news/item/10-10-2023-monitoring-air-pollution-levels-is-key-to-adopting-and-implementing-who-s-global-air-quality-guidelines**, (accessed 2 May 2024).
2 M. L. Grilli, *Metals*, 2020, **10**, 820.
3 R. J. Rath, S. Farajikhah, F. Oveissi, F. Dehghani and S. Naficy, *Adv. Eng. Mater.*, 2023, **25**, 2200830.
4 J. Chen, C. Burger, C. V. Krishnan and B. Chu, *J. Am. Chem. Soc.*, 2005, **127**, 14140–14141.
5 A. Umar, A. A. Ibrahim, R. Kumar, H. Algadi, H. Albargi, M. A. M. Alhamami, U. T. Nakate and S. Baskoutas, *Sci. Adv. Mater.*, 2021, **13**, 724–733.
6 A. Umar, J. Singh, A. A. Ibrahim, R. Kumar, P. Rai, A. K. Rai, H. Algadi, M. A. M. Alhamami and M. M. E. Elsddig, *Sci. Adv. Mater.*, 2021, **13**, 2358–2363.
7 X. C. Song, Y. F. Zheng, E. Yang and Y. Wang, *Mater. Lett.*, 2007, **61**, 3904–3908.
8 X. Gao, X. Su, C. Yang, F. Xiao, J. Wang, X. Cao, S. Wang and L. Zhang, *Sens. Actuators, B*, 2013, **181**, 537–543.

9 H. Zheng, J. Z. Ou, M. S. Strano, R. B. Kaner, A. Mitchell and K. Kalantar-zadeh, *Adv. Funct. Mater.*, 2011, **21**, 2175–2196.

10 S. Vallejos, P. Umek, T. Stoycheva, F. Annanouch, E. Llobet, X. Correig, P. De Marco, C. Bittencourt and C. Blackman, *Adv. Funct. Mater.*, 2013, **23**, 1313–1322.

11 Y.-T. Hsieh, L.-W. Chang, C.-C. Chang and H. C. Shih, *Electrochem. Solid-State Lett.*, 2011, **14**, K40.

12 E. Rossinyol, J. Arbiol, F. Peiró, A. Cornet, J. R. Morante, B. Tian, T. Bo and D. Zhao, *Sens. Actuators, B*, 2005, **109**, 57–63.

13 B. Tian, X. Liu, L. A. Solovyov, Z. Liu, H. Yang, Z. Zhang, S. Xie, F. Zhang, B. Tu, C. Yu, O. Terasaki and D. Zhao, *J. Am. Chem. Soc.*, 2004, **126**, 865–875.

14 A. Rumplecker, F. Kleitz, E.-L. Salabas and F. Schüth, *Chem. Mater.*, 2007, **19**, 485–496.

15 M. Hafeez, A. Siddique Saleemi, S. Ur Rehman, M. Adrees, S. Mehmood, I. A. Mir and L. Zhu, *Appl. Surf. Sci.*, 2021, **536**, 147713.

16 W. B. Carter, G. W. Book, T. A. Polley, D. W. Stollberg and J. M. Hampikian, *Thin Solid Films*, 1999, **347**, 25–30.

17 G. Carta, N. El Habra, L. Crociani, G. Rossetto, P. Zanella, A. Zanella, G. Paolucci, D. Barreca and E. Tondello, *Chem. Vap. Deposition*, 2007, **13**, 185–189.

18 D. Barreca, G. Carraro, E. Fois, A. Gasparotto, F. Gri, R. Seraglia, M. Wilken, A. Venzo, A. Devi, G. Tabacchi and C. Maccato, *J. Phys. Chem. C*, 2018, **122**, 1367–1375.

19 S. Blittersdorf, N. Bahlawane, K. Kohse-Höinghaus, B. Atakan and J. Müller, *Chem. Vap. Deposition*, 2003, **9**, 194–198.

20 M. Lugo-Ruelas, P. Amézaga-Madrid, O. Esquivel-Pereyra, W. Antúnez-Flores, P. Pizá-Ruiz, C. Ornelas-Gutiérrez and M. Miki-Yoshida, *J. Alloys Compd.*, 2015, **643**, S46–S50.

21 D. Barreca, G. Carraro, A. Gasparotto, C. Maccato, R. Seraglia and G. Tabacchi, *Inorg. Chim. Acta*, 2012, **380**, 161–166.

22 H. Meixner and U. Lampe, *Sens. Actuators, B*, 1996, **33**, 198–202.

23 C. Zhang, Y. Luo, J. Xu and M. Debliquy, *Sens. Actuators, A*, 2019, **289**, 118–133.

24 F. E. Annanouch, Z. Haddi, S. Vallejos, P. Umek, P. Guttmann, C. Bittencourt and E. Llobet, *ACS Appl. Mater. Interfaces*, 2015, **7**, 6842–6851.

25 F. E. Annanouch, Z. Haddi, M. Ling, F. Di Maggio, S. Vallejos, T. Vilic, Y. Zhu, T. Shujah, P. Umek, C. Bittencourt, C. Blackman and E. Llobet, *ACS Appl. Mater. Interfaces*, 2016, **8**, 10413–10421.

26 E. Navarrete, C. Bittencourt, P. Umek, D. Cossement, F. Güell and E. Llobet, *J. Alloys Compd.*, 2020, **812**, 152156.

27 È. Navarrete, C. Bittencourt, X. Noirfalise, P. Umek, E. González, F. Güell and E. Llobet, *Sens. Actuators, B*, 2019, **298**, 126868.

28 E. Navarrete, C. Bittencourt, P. Umek and E. Llobet, *J. Mater. Chem. C*, 2018, **6**, 5181–5192.

29 P. Velusamy, R. Xing, R. R. Babu, E. Elangovan, J. Viegas, S. Liu and M. Sridharan, *Sens. Actuators, B*, 2019, **297**, 126718.

30 P. Velusamy, R. Ramesh Babu, M. Sathiya, A. Ahmad, A. A. Alothman, M. Sheikh Saleh Mushab, E. Elamurugu, M. Senthil Pandian and P. Ramasamy, *New J. Chem.*, 2022, **46**, 22469–22485.

31 V. Periyasamy, R. R. Babu, A. Ahmad, M. D. Albaqami, R. G. Alotabi and E. Elamurugu, *ACS Omega*, 2022, **7**, 35191–35203.

32 V. P, X. Liu, R. Ramesh Babu, M. Sathiya, N. Salem Alsaiari, F. Mohammed Alzahrani, M. Tariq Nazir, E. Elamurugu and F. Zhang, *Chemosphere*, 2023, **329**, 138535.

33 S. B. Malik, E. Llobet and F. E. Annanouch, in *Eurosensors 2023*, MDPI, Basel Switzerland, 2024, vol. 97, p. 133.

34 S. B. Malik, K. V. Mejia-Centeno, P. R. Martínez-Alanis, A. Cabot, F. Güell, F. E. Annanouch and E. Llobet, *Sens. Actuators, B*, 2024, **400**, 134879.

35 S. B. Malik, F. E. Annanouch and E. Llobet, in *2023 IEEE Sensors, IEEE*, 2023, pp. 1–4.

36 S. B. Malik, F. E. Annanouch and E. Llobet, *Chemosensors*, 2023, **11**, 550.

37 S. Agarwal, P. Rai, E. N. Gatell, E. Llobet, F. Güell, M. Kumar and K. Awasthi, *Sens. Actuators, B*, 2019, **292**, 24–31.

38 C. Wang, L. Yin, L. Zhang, D. Xiang and R. Gao, *Sensors*, 2010, **10**, 2088–2106.

39 V. B. Kamble and A. M. Umarji, *RSC Adv.*, 2015, **5**, 27509–27516.

40 S. Yang, G. Lei, H. Xu, Z. Lan, Z. Wang and H. Gu, *Nanomaterials*, 2021, **11**, 1026.

41 D. Y. Nadargi, A. Umar, J. D. Nadargi, S. A. Lokare, S. Akbar, I. S. Mulla, S. S. Suryavanshi, N. L. Bhandari and M. G. Chaskar, *J. Mater. Sci.*, 2023, **58**, 559–582.

42 F. Quaranta, R. Rella, P. Siciliano, S. Capone, M. Epifani, L. Vasanelli, A. Licciulli and A. Zocco, *Sens. Actuators, B*, 1999, **58**, 350–355.

43 S. Capone, M. Epifani, F. Quaranta, P. Siciliano and L. Vasanelli, *Thin Solid Films*, 2001, **391**, 314–319.

44 J. Pan, A. Yang, D. Wang, J. Chu, F. Lei, X. Wang and M. Rong, *IEEE Trans. Instrum. Meas.*, 2022, **71**, 1–8.

45 L. Zhao, F. Tian, J. Qian, H. Li and Z. Wu, *IEEE Trans. Instrum. Meas.*, 2023, **72**, 1–9.

46 Z. Ye, Y. Liu and Q. Li, *Sensors*, 2021, **21**, 7620.

47 H. Chen, D. Huo and J. Zhang, *IEEE Trans. Biomed. Circuits Syst.*, 2022, **16**, 169–184.

48 N. Ha, K. Xu, G. Ren, A. Mitchell and J. Z. Ou, *Advanced Intelligent Systems*, 2020, **2**, 2000063.

49 I. T. Jolliffe and J. Cadima, *Philos. Trans. R. Soc., A*, 2016, **374**, 20150202.

50 K. Zhou and Y. Liu, *Sensors*, 2021, **21**, 4826.

51 S. H. Wang, T. I. Chou, S. W. Chiu and K. T. Tang, *IEEE Sens. J.*, 2021, **21**, 6401–6407.

52 Md. S. I. Sagar, N. R. Allison, H. M. Jalajamony, R. E. Fernandez and P. K. Sekhar, *J. Electrochem. Soc.*, 2022, **169**, 127512.